

Regional cloud characteristics over the tropical northwestern Pacific as revealed by Tropical Rainfall Measuring Mission (TRMM) Precipitation Radar and TRMM Microwave Imager

Myung-Sook Park,¹ Yong-Sang Choi,¹ Chang-Hoi Ho,¹ Chung-Hsiung Sui,² Seon Ki Park,³ and Myoung-Hwan Ahn⁴

Received 25 April 2006; revised 20 June 2006; accepted 4 August 2006; published 10 March 2007.

[1] The present study investigates regional cloud characteristics over the tropical northwestern Pacific using Tropical Rainfall Measuring Mission (TRMM) data sets such as rain rate, radar reflectivity, and passive microwave radiometer polarization corrected temperature (PCT). In particular, the tropical northwestern Pacific is divided into two surface rain maxima regions: the South China Sea (SCS) and the Philippine Sea (PS). The TRMM variables are retrieved by a pair of spaceborne microwave sensors, Precipitation Radar (PR) and TRMM Microwave Imager (TMI). It is revealed that the SCS contains more frequent deeply developed convective systems relative to the PS on the basis of the analysis of the PR and TMI version-6 data during a 4-year period (1998–2001) of summers. This is mainly indicated by two factors: strong PR reflectivity (≥ 30 dBZ) above the freezing level (~ 5 km) and TMI ice-scattering signature (PCT at 85.5 GHz $\leq \sim 190$ K, and PCT at 37.0 GHz $\leq \sim 260$ K), which are more frequent over the SCS than over the PS. Comparison of TMI and PR rain rates, a relatively small (large) positive PR–TMI bias is observed for an average of rainy areas over the SCS (PS). This region-dependent PR–TMI bias can arise from the regionally different extents of both (1) the PR’s underestimate by attenuation correction and (2) the TMI’s overestimate by emission from the melting layer (i.e., SCS > PS in (1) and (2)). These differences are due to the excess of heavy rainfall events, high rain rates, strong convective intensities, and high cloud top heights in the SCS compared with the PS.

Citation: Park, M.-S., Y.-S. Choi, C.-H. Ho, C.-H. Sui, S. K. Park, and M.-H. Ahn (2007), Regional cloud characteristics over the tropical northwestern Pacific as revealed by Tropical Rainfall Measuring Mission (TRMM) Precipitation Radar and TRMM Microwave Imager, *J. Geophys. Res.*, *112*, D05209, doi:10.1029/2006JD007437.

1. Introduction

[2] The precipitation process is closely linked to large-scale circulation, radiation budget, and energy cycle of the atmosphere over the globe. Accordingly, the validation of rainfall is one of the most important elements in evaluating climate models. However, there are many difficulties in acquiring the “true value” of rainfall and its distribution due to strong variability in spatial and temporal domains. The most feasible way is to utilize information retrieved from satellites combined with accessible rain gauge networks [Simpson *et al.*, 1996]. In this extension, substantial progress in observing global precipitation has been made by several satellite projects. The Tropical Rainfall Measuring Mission (TRMM) is one of those efforts.

[3] The TRMM satellite has been successfully operating during the past nine years (1998–present). One of its main purposes is to obtain three-dimensional distributions of rain rate and latent heat release over the tropics [Simpson *et al.*, 1988; Kummerow *et al.*, 1998]. The TRMM satellite carries the first spaceborne active radar, the Precipitation Radar (PR), together with a passive microwave imager, the TRMM Microwave Imager (TMI).

[4] The PR and TMI rain products are produced independently with different physical principles and retrieval algorithms. The PR rain is produced by means of an empirical relation between satellite-observed attenuated-corrected reflectivity (hereafter, reflectivity) and ground truth rain rate, which is similar to the application used for ground-based radar [Iguchi *et al.*, 2000]. Namely, the PR directly extracts the vertical profile of the rain rate. On the other hand, the TMI provides rain products rather indirectly. The TMI estimates optimal rain products by a comparison between the observed microwave brightness temperature (TB) and the calculated microwave TB from a radiative transfer model [Kummerow *et al.*, 2001].

[5] Previous studies have documented that the PR and TMI rain products produce a systematic disagreement, predominantly over the tropical oceans. Masunaga *et al.* [2002] found that this disagreement is widely distributed

¹School of Earth and Environmental Sciences, Seoul National University, Seoul, Korea.

²Institute of Hydrological Sciences, National Central University, Jhongli, Taiwan.

³Department of Environmental Science and Engineering, Ewha Womans University, Seoul, Korea.

⁴Meteorological Research Institute, Korea Meteorological Administration, Seoul, Korea.

over the entire tropics and suggested that it may result from an inherent dissimilarity of the two rain products, such as their different observing systems and retrieval algorithms. Some studies have also compared the two rain products with regard to regional differences. *Masunaga et al.* [2002] showed that the discrepancy of rainfall (TMI minus PR) is greater over the tropical ocean (15°S–15°N) than elsewhere. Further, *Berg et al.* [2002] presented that greater discrepancy is found over the tropical west Pacific compared to the tropical east Pacific. *Nesbitt et al.* [2004] documented that the region-dependent biases are caused by different horizontal and vertical morphologies of precipitating systems.

[6] Interestingly, *Takahashi* [2006] issued tables of the regional difference of cloud and rain systems over the tropical northwestern Pacific (TNP). He analyzed data obtained from videosondes and witnessed that different rain regimes exist in the TNP. In regions near a continent, a large amount of graupel is observed, thus indicating that a cold rain process is dominant there. On the other hand, much fewer graupels are observed in the open sea far from a continent, implying that the cold rain process is much less dominant. Those findings suggest that the TNP may be distinguished by two different convection (and/or precipitation process) regimes.

[7] The foregoing results were mostly inferred from the earlier version (version 5) of TRMM data. In the latest version (version 6) of the TRMM data sets, most of the parameters were reproduced with some changes, such as attenuation correction and surface clutter range [*TRMM PR Team*, 2005]. *Song et al.* [2004] showed that the PR–TMI bias has been reduced significantly in version 6. It is therefore expected that the version change may have some influence on the bias results. The present study attempts to apprehend the regional cloud characteristics over the TNP by using the PR and TMI rain products in version 6. For this purpose, cloud characteristics over the TNP will be compared in two subregions of maximal rain rates: the South China Sea (SCS, 110°–120°E, 5°–20°N) and the Philippine Sea (PS, 130°–140°E, 5°–20°N). We analyze the frequency of PR reflectivity and TMI ice scattering signature derived from the microwave TBs over the two regions to understand cloud characteristics closely linked to both rain rate distributions and rain rate discrepancies between the PR and TMI. The cloud top properties over the two regions are also examined by applying hourly infrared (IR) data from the Geostationary Meteorological Satellite-5 (GMS-5).

[8] This paper is organized as follows: the data sets and method are described in section 2; the climatological features of rain rates and large-scale environments over TNP are presented in section 3; in section 4, the PR and TMI rainfall as well as the PR reflectivity and the TMI ice scattering signatures are compared over the SCS and PS; in section 5, the regional difference of cloud characteristics in the two regions is interpreted on the basis of the results from the TRMM along with the climatological features; and finally, the results are summarized in section 6.

2. Data and Method

[9] Three primary TRMM orbital data sets for version 6 are used in this study: (1) reflectivity and near-surface rain

rate in the PR profiles (2A25), (2) near-surface rain rate in the TMI profiles (2A12), and (3) microwave TBs in the TMI Level-1B data (1B11). The 2A25 data set contains volumetric PR reflectivity at 13.8 GHz and rain rates from near surface to 20 km within a 215 km narrow swath. Horizontal and vertical resolutions of the PR data are 4.3 km and 250 m at nadir, respectively. The TMI 2A12 algorithm uses observations from all the TMI frequencies (10.7, 19.3, 21.3, 37.0, and 85.5 GHz, dual polarized except for 21.3 GHz) within a 760 km wide swath. The sampling rate is the same as that of the 85-GHz fields of view (FOV) ($=7 \times 5$ km) in the TMI 2A12 data set, but the retrieved rain rate does not have such a good resolution. The actual resolution is much coarser than that because the 2A12 algorithm uses all the frequency channels including 10.7 GHz with a low resolution ($=60 \text{ km} \times 60 \text{ km}$). As a result, the TMI rain rate introduces a significant beam-filling issue, which is one of the factors to induce rain rates discrepancies between the TMI and the PR [*Nesbitt et al.*, 2004]. The 1B11 data set contains TMI-calibrated TBs at five frequencies. Among those nine channels, 37.0 and 85.5 GHz are selectively examined in this study because they are known to respond to ice scattering sensitively [*Wu and Weinman*, 1984; *Wilheit*, 1986; *Spencer et al.*, 1989; *Cecil et al.*, 2002]. The TMI TBs at 37.0 and 85.5 GHz (TB₃₇ and TB₈₅) have effective fields of view (FOV) of $16 \text{ km} \times 9 \text{ km}$ and $7 \text{ km} \times 5 \text{ km}$, respectively (see *Kummerow et al.* [2000] for details).

[10] In the present study, we compare the rainfall over the SCS and PS by using the PR and TMI near-surface rain rates in the TRMM orbital data sets. In the comparison, the PR–TMI bias is accounted for. Next, the PR reflectivity profiles and the TMI microwave TBs are examined to identify cloud characteristics. It is well known that radar reflectivity depends on the hydrometeor diameter, number, and phase, etc. As a result, PR reflectivity at 13.8 GHz (2.2-cm wavelength) responds to drops smaller than about 3 mm in the Rayleigh scattering regime. The largest raindrops, graupel, and hail are active in the Mie scattering regime. Concerning the dependency of PR reflectivity on phase, liquid drops have a reflectivity which is 7 dBZ greater than the potential for ice particles with the same size, because of their different dielectric properties [*Cecil et al.*, 2002].

[11] Regarding the TMI, precipitation-sized ice reduces the observed microwave TB by scattering because of its shorter wavelength, 85.5 GHz (3.5-mm wavelength) and 37.0 GHz (8.1-mm wavelength). This result is regarded as an ice scattering signature that depends on optical depth. In detail, particles with diameter ($> \sim 0.1$ mm) and diameter O(mm) are in the Mie regime at 85.5 GHz and 37.0 GHz, respectively [*Cecil et al.*, 2002]. Emission by water also contributes to the TB, but it is a secondary factor for those scattering channels [*Spencer et al.*, 1989].

[12] We also use two other TRMM data sets: (1) gridded near-surface rain rates in the PR monthly average (3A25) and (2) lightning flash density from the Lightning Imager Sensor (LIS in *Christian et al.* [1999]). Firstly, monthly averaged rain rates with a $0.5^\circ \times 0.5^\circ$ grid of 3A25 are compared with corresponding nongridded products in 2A25. Secondly, the LIS retrieves lightning with FOV of $600 \text{ km} \times 600 \text{ km}$ by recording optical pulses in the near-IR. Its horizontal resolution is of the order of 5 km.

Table 1. Typhoon-Passing History Over Either the South China Sea or the Philippine Sea in the Summers (June–July–August) of 1998–2001

Year	Typhoon
1998	Nichole (7/8), Otto (8/1~8/3), Penny (8/6~8/11), Rex (8/24)
1999	Maggie (6/1~6/6), Neil (7/23~7/26), Olga (7/29~7/31), Paul (8/3), Rachel (8/5~8/6), Sam (8/17~8/22)
2000	Kirogi (7/2~7/5), Kai-tak (7/3~7/8), Bolaben (7/24), Ewiniar (8/10), Bilis (8/18~8/22), Kaemi (8/19~8/22), Prapiroon (8/24~8/27), Maria (8/27~8/31)
2001	Chebi (6/19~6/22), Durián (6/29~7/2), Utor (7/1~7/5), Trami (7/8~7/11), Yutu (7/22~7/26), Toraji (7/25~7/29), Usagi (8/8~8/10), Pabuk (8/16~8/17), Wutip (8/26~8/27), Fitow (8/28~8/31)

Lightning density is a useful indicator to diagnose the intensity of convection and precipitation features [Cecil *et al.*, 2002]. The LIS data is obtained from the Global Hydrology Resource Center website (<http://ghrc.msfc.nasa.gov>).

[13] In calculating the rain rate in 3A25 and the orbital rain products (2A12 and 2A25), the area means of rain rates are obtained by averaging either all grids or rainy grids only (i.e., nonzero rain rate grids). The former and latter area means are termed “unconditional” and “conditional” rain rate averages, respectively. All the rain-related TRMM products are available at the NASA website (<http://trmm.gsfc.nasa.gov/>).

[14] In addition, non-TRMM products are examined to explore the background states in the TNP. We inquire into the precipitation and sea surface temperature (SST) states by using the Climate Prediction Center Merged Analysis of Precipitation (CMAP compiled by Xie and Arkin [1997]) and monthly optimally interpolated SST archived at the National Centers for Environmental Prediction (NCEP) [Reynolds and Smith, 1994]. Various climate parameters such as atmospheric temperature, moisture, and wind field are taken from the NCEP/National Center for Atmospheric Research (NCAR) reanalysis [Kalnay *et al.*, 1996]. The monthly NCEP/NCAR reanalysis data have 17 vertical layers with a horizontal resolution of $2.5^\circ \times 2.5^\circ$, which is the same as the CMAP and SST data. Furthermore, we use the GMS-5 IR TB at $10.8 \mu\text{m}$ for supplementary IR information such as cloud top height and temperature. The original spatial and temporal resolution of the GMS-5 data is about 5 km and 1 hour, respectively. The data were converted into daily average data with a $0.25^\circ \times 0.25^\circ$ grid resolution.

[15] All the data used in this study are within the TNP during summer (June–July–August, hereafter JJA) for the 1998–2001 period. We are particularly concerned about frequent occurrence of tropical cyclones in the TNP during this period, which disorders the general cloud characteristics. Therefore we exclude the tropical cyclone days from our analysis (see Table 1). As a result, the analysis is accomplished for 264 days only (about 4000 orbits of TRMM). The typhoon history is obtained from the Regional Specialized Meteorological Centers-Tokyo Tropical Cyclone Center.

3. Rainfall and Large-Scale Environments

[16] We start with a discussion on the rainfall and large-scale environments that are taken from the CMAP and NCEP/NCAR reanalysis, respectively. Figure 1a depicts the JJA-mean CMAP precipitation (mm d^{-1}) for the

period 1998–2001 over the TNP. Heavy rainfall regions ($\geq 8 \text{ mm d}^{-1}$) are broadly distributed over the domain. Clearly, rainfall maximum greater than 14 mm d^{-1} is found over two regions such as SCS and PS. The average values of CMAP rainfall over the SCS and PS are 10.3 and 11.5 mm d^{-1} , respectively. From a global perspective, these two heavy rainfall regions are relevant to a northward transition of the Intertropical Convergence Zone (ITCZ) during JJA. The precipitation band is elongated toward East Asia and thus linked to the East Asian summer monsoon.

[17] Figures 1b–1d illustrate some large-scale environments, e.g., SST, relative vorticity at 850 hPa, and vertical velocity at 500 hPa as the JJA mean state. In general, most of the TNP is covered by SSTs higher than 29°C , which is referred to as a “warm pool” (Figure 1b). The averaged SSTs over the SCS and PS have similar values of about 29.6°C . Corresponding to this high SST, the overlying atmosphere tends to attain a potentially unstable condition, and strong surface winds induce exchanges of heat and moisture. This implies that deep convection can be developed if favorable dynamic conditions (i.e., positive low-level relative vorticity associated with strong vertical velocities) are provided.

[18] Positive 850-hPa relative vorticity is found over the SCS, PS, and southeastern Asia between 10°N and 20°N (Figure 1c). The averaged relative vorticities over the SCS and PS are 0.29 and 0.02 in 10^{-5} s^{-1} , respectively. Most of these positive values result from an enhanced moisture convergence in conjunction with a northward movement of the ITCZ from the equator. The vertical velocity at 500 hPa also presents a similar spatial distribution consistent with the 850-hPa relative vorticity (Figure 1d). For the domain-averaged vertical velocity, values over the SCS are 0.2 hPa d^{-1} higher compared to the PS, so that the synoptic-scale vertical motion over the SCS is slightly stronger. In general, most of the areas of strong rising motion ($< -50 \text{ hPa d}^{-1}$) cover positive relative vorticity regions (Figures 1c and 1d). However, areas of relatively weak rising motion ($> -40 \text{ hPa d}^{-1}$) are found even in negative relative vorticity regions along the equator. These spatial distributions of the two dynamic variables involved result in the equatorial regions being conditionally unstable and producing many occasional showers, although the season mean relative vorticity is negative.

[19] Two thermodynamic parameters, equivalent potential temperature (θ_e) and saturated equivalent potential temperature (θ_e^*), are commonly used to diagnose atmospheric instability. The atmosphere is conditionally unstable if $\partial\theta_e^*/\partial z$ is negative in the lower troposphere. The air near the surface has a sufficiently high value of θ_e , so that an air parcel forcibly raised from the boundary layer becomes buoyant as it ascends to saturation. The distributions of the JJA-mean θ_e and θ_e^* , averaged over the SCS, PS, and the east Pacific (120°W – 150°W , 5°S – 15°N), are displayed in Figure 2. The east Pacific record is used as a further example for comparing our analysis domain to a more stable region [Berg *et al.*, 2002]. It is clearly found that the atmosphere over the SCS and PS is conditionally unstable. Interestingly, the SCS and PS have an almost parallel vertical profile for both θ_e and θ_e^* , while the eastern Pacific does not as a result of the trade inversion by the descending branch of the Walker circulation. Relatively higher θ_e and θ_e^* are observed over the SCS compared to the PS.

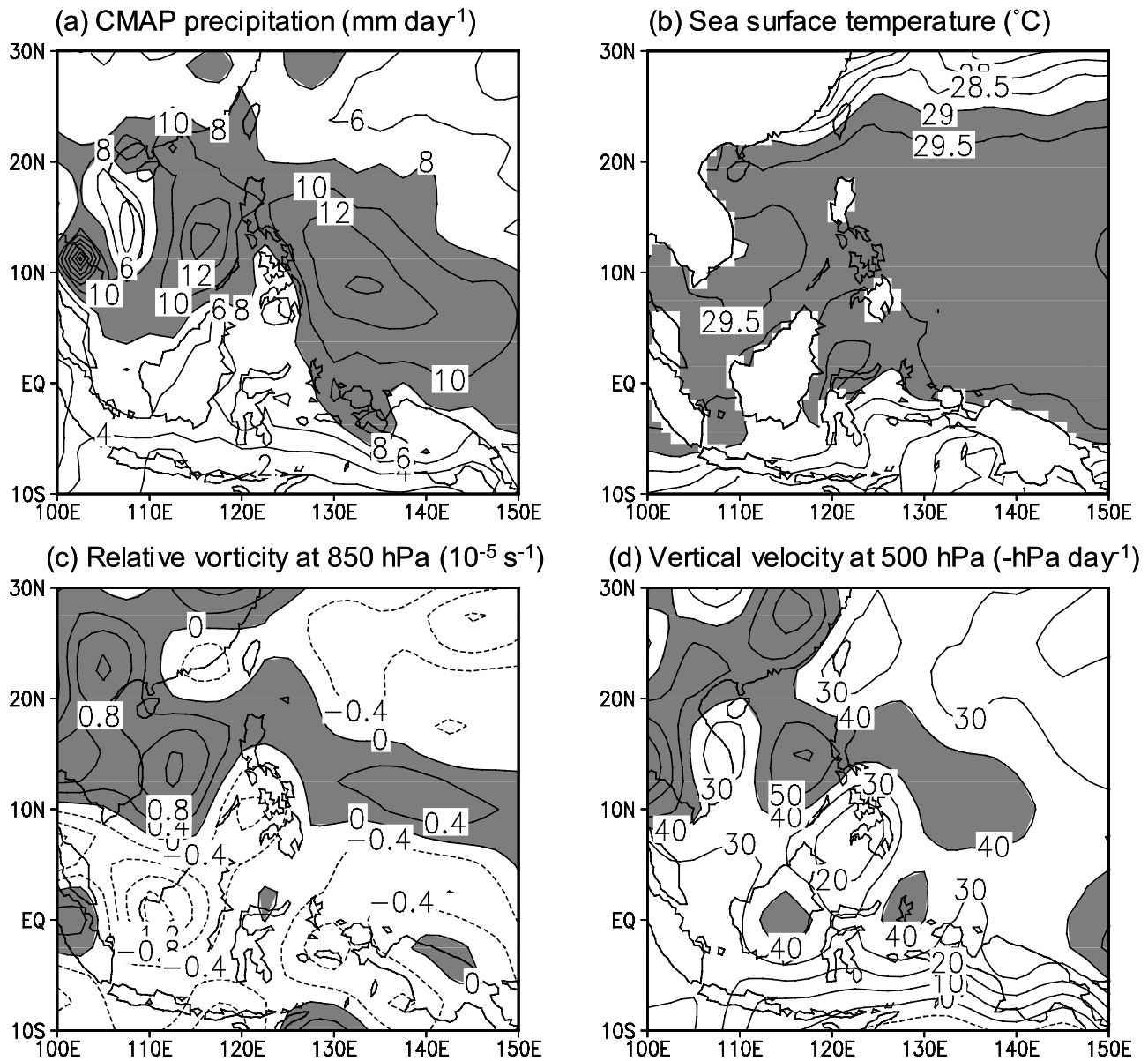


Figure 1. (a) June–July–August (JJA) mean distribution of Climate Prediction Center Merged Analysis of Precipitation (CMAP) precipitation (mm d^{-1}), (b) sea surface temperature ($^{\circ}\text{C}$), (c) relative vorticity at 850 hPa (10^{-5} s^{-1}), and (d) vertical velocity at 500 hPa ($-\text{hPa d}^{-1}$) over the tropical northwestern Pacific (TNP) during the years 1998–2001.

[20] On the whole, abundant amounts of rainfall occur over the TNP due to high SST and thermodynamically unstable environments. The dominance of SCS relative to PS is also found in the fields of vertical velocity and relative vorticity, although precipitation is conversely higher over PS, and mean SSTs over the two regions are similar. In the following section we examine the cloud characteristics focused over the SCS and PS, using TRMM observations.

4. Rain Rates and Cloud Characteristics in TRMM Observations

4.1. Rain Rates From TMI and PR

[21] As described in section 2, the average of unconditional rain rates includes rainless grids, while that of

conditional rain rates counts rain grids only. It is found that many grids identified as rainless from the TMI have nonzero rain rates from the PR, while the opposite is hardly observed (figure not shown). In other words, the PR is more sensitive than the TMI to the existence of rainfall over the TNP. The different sensitivities of rainfall between TMI and PR are partially ascribable to the spatial resolution difference, but are also due to the rain/no-rain screening used by the TMI 2A12 algorithm. The 2A12 algorithm assumes that rain rate is zero where liquid water path is less than a certain critical value. This artificial screening could force the TMI algorithm to ignore potentially raining clouds [Berg *et al.*, 2006].

[22] Figures 3a and 3b show the unconditional JJA-mean rain rates derived by the PR 2A25 and TMI 2A12, respec-

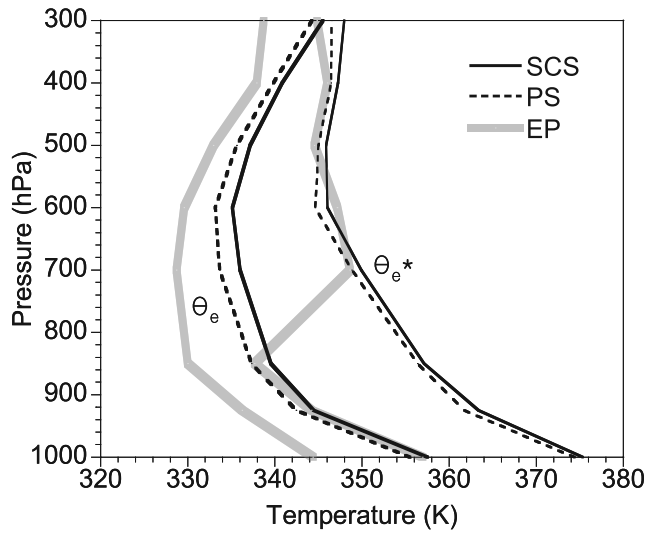


Figure 2. Vertical structures of equivalent potential temperature (θ_e) and saturated equivalent potential temperature (θ_e^*) over the South China Sea (solid line), the Philippine Sea (dashed line), and the east Pacific (gray solid line).

tively. The resolution of Figure 3 is to $1^\circ \times 1^\circ$ such that it is not so full of sampling noise. Both rainfalls show comparable distributions for the centers of maximal rainfall as well as similar magnitudes: the maxima of rain rates locate over the SCS and PS. However, these two rain rates in the heavy rainfall regions ($\geq 8 \text{ mm d}^{-1}$) are not as large as that of CMAP (compare with Figure 1a). The excess of CMAP over PR (or TMI) is about 4 mm d^{-1} in the SCS and PS (Table 2). This may be related to the exclusion of typhoon effects in calculating averages in PR or TMI. On the other hand, it is noted that the unconditional rain rates for both PR and TMI are consistently higher over the PS than over the SCS (5.65 versus 7.53 in PR and 5.58 versus 6.58 in TMI).

[23] The conditional means from the PR and TMI are presented in Figures 3c and 3d, respectively. These conditional means are higher than the unconditional means, since rainless grids are not included in the calculation. Not surprisingly, the conditional rain rate is generally higher near/in continents than oceanic areas because its average, in the temporal and spatial domain, implies a high intensity of rainfall (Figures 3c and 3d). Therefore contrary to the unconditional rain, the conditional rain rate is much higher over SCS. The discrepancies between the SCS and PS are $5.67 (=63.82-58.15) \text{ mm d}^{-1}$ and $10.09 (=58.83-48.74) \text{ mm d}^{-1}$ for PR and TMI, respectively (Table 2). In

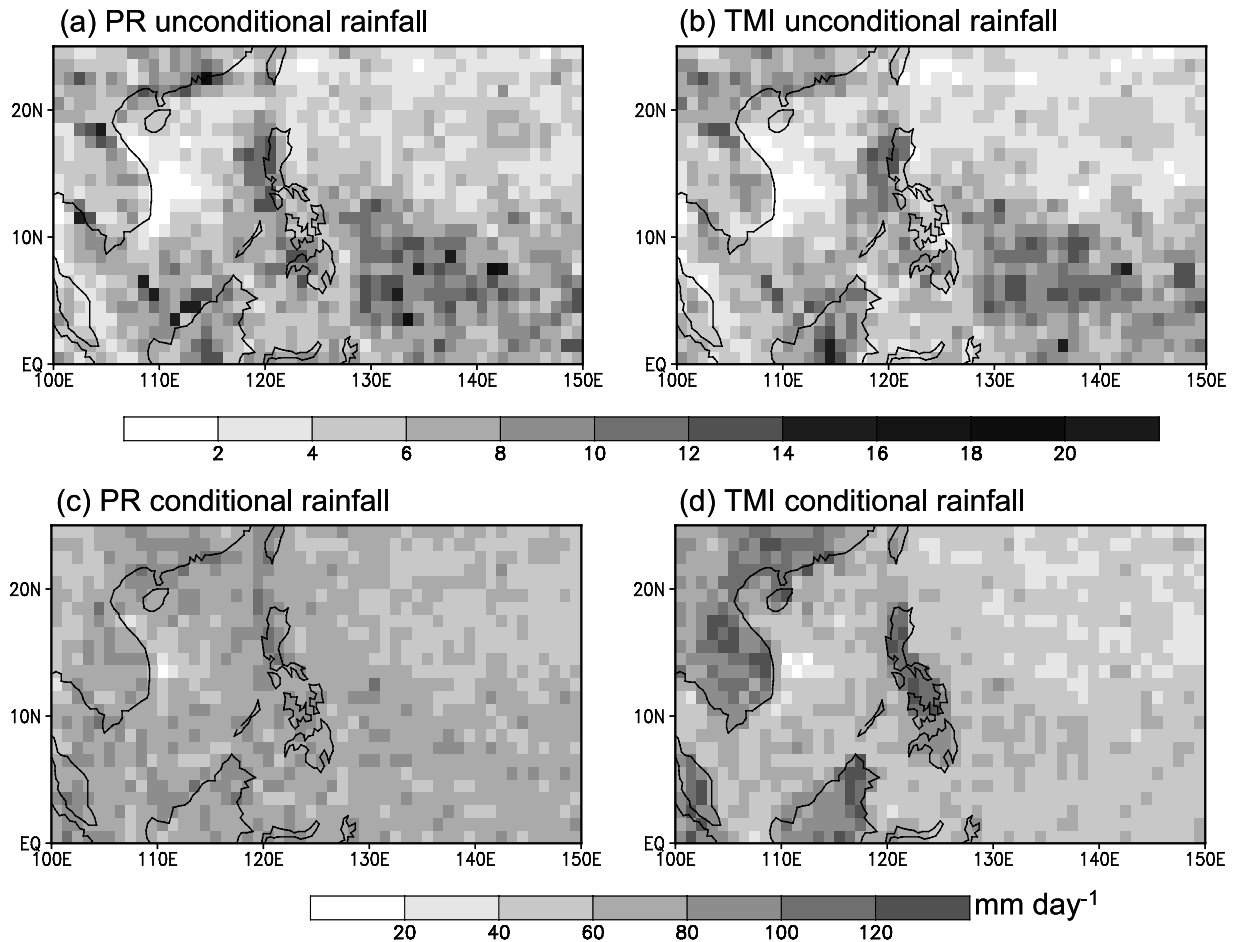


Figure 3. Near-surface rain rates (mm d^{-1}) in unconditional mean of (a) Precipitation Radar (PR) and (b) TRMM Microwave Imager (TMI) and in conditional mean of (c) PR and (d) TMI in JJA of the years 1998–2001 (see text for more details).

Table 2. Mean Values of TRMM Microwave Imager (TMI), Precipitation Radar (PR) Rain Parameters, Climate Prediction Center Merged Analysis of Precipitation (CMAP) Precipitation, and Lightning Imager Sensor (LIS) Lightning Density for the South China Sea and the Philippine Sea^a

Variables	SCS	PS
CMAP precipitation, mm d ⁻¹	10.32	11.52
PR 2A25 near-surface rain rate (unconditional), mm d ⁻¹	5.65	7.53
TMI 2A12 near-surface rain rate (unconditional), mm d ⁻¹	5.58	6.58
PR 2A25 near-surface rain rate (conditional), mm d ⁻¹	63.82	58.83
TMI 2A12 near-surface rain rate (conditional), mm d ⁻¹	58.15	48.74
PR 3A25 near-surface rain rate (unconditional), mm d ⁻¹	6.72	8.16
PR 3A25 near-surface rain rate (conditional), mm d ⁻¹	70.32	66.96
LIS lightning density, km ⁻² d ⁻¹	0.023	0.005

^aWhen comparing the two regions, large values are indicated by bold font.

further analysis, with storm height in PR3A25, storms are much deeper over the SCS than over the PS (figure not shown). Combining the results discussed above, it is suggested that the intensity of rainfall is certainly stronger for rainy areas of the SCS because of intense convection compared to the PS.

[24] Besides, the PR–TMI rain bias is shown predominantly in the conditional rainfall means; the PR rainfall is higher than the TMI rainfall over the whole TNP (compare Figures 3c and 3d). The PR–TMI conditional rain bias is 5.67 (10.09) mm d⁻¹ in SCS (PS), so that it is actually region dependent (Table 2). The PR is biased high 8.88 (17.15) % relative to the TMI. This can be accounted for by the contoured log frequency diagrams of TMI versus PR rainfall over the TNP (Figure 4). In Figure 4, a histogram bin is set to 10^{0.05} times the axis value and a contour value of $-x$ indicates the value of a fraction of 1/10^{-x} of the distribution. The median of the histogram of PR rainfall as a

function of TMI rainfall is also plotted (thick solid line) with the 1:1 (thin solid line) and 2:1 (thin dashed line) bias lines [Nesbitt *et al.*, 2004]. As seen in the median line (thick solid line) in Figure 4, the PR rainfall predominates over the TMI rainfall by less than about 20 mm d⁻¹, which makes a higher conditional-averaged rain rate for the PR. Conversely, the TMI tends to overestimate heavy rainfall (Figure 4). As opposed to the above results from conditional rainfall, the PR–TMI bias in unconditional rainfall is not clear; it is less than 1 mm d⁻¹, which covers less than 10% of rain rates (Table 2). This value is actually small compared to the results from version 5 in many previous studies [e.g., Kummerow *et al.*, 2000; Masunaga *et al.*, 2002].

[25] The near-surface rain rate from the PR3A25 is also examined in Table 2. This monthly average PR3A25, contrary to the calculation of PR2A25, includes the rainfall for typhoon activities. The PR3A25 unconditional rain rates are about 3.5 mm d⁻¹ (10.32 versus 6.72 in SCS and 11.52 versus 8.16 in PS) lower than CMAP precipitation. Here, PR may be more reliable in retrieving rain rate, for the reason that the PR echoes evaluate rainfall more directly than other satellites which participate in CMAP precipitation [Xie and Arkin, 1997]. In comparison with PR2A25, the unconditional rainfall is about 1 mm d⁻¹ higher than PR3A25. However, the conditional rainfall is about 12% times higher than PR2A25. This excess in rainfall of PR3A25 over PR2A25 implies that tropical cyclones enhance a large portion of precipitation for rainy areas over TNP.

[26] It is noted that rain rates are actually estimated from either actively and passively sensed algorithms, adopting radar reflectivity and microwave TB respectively, while the other two methods respond to a number of factors concerned with hydrometeors. Accordingly, the foregoing

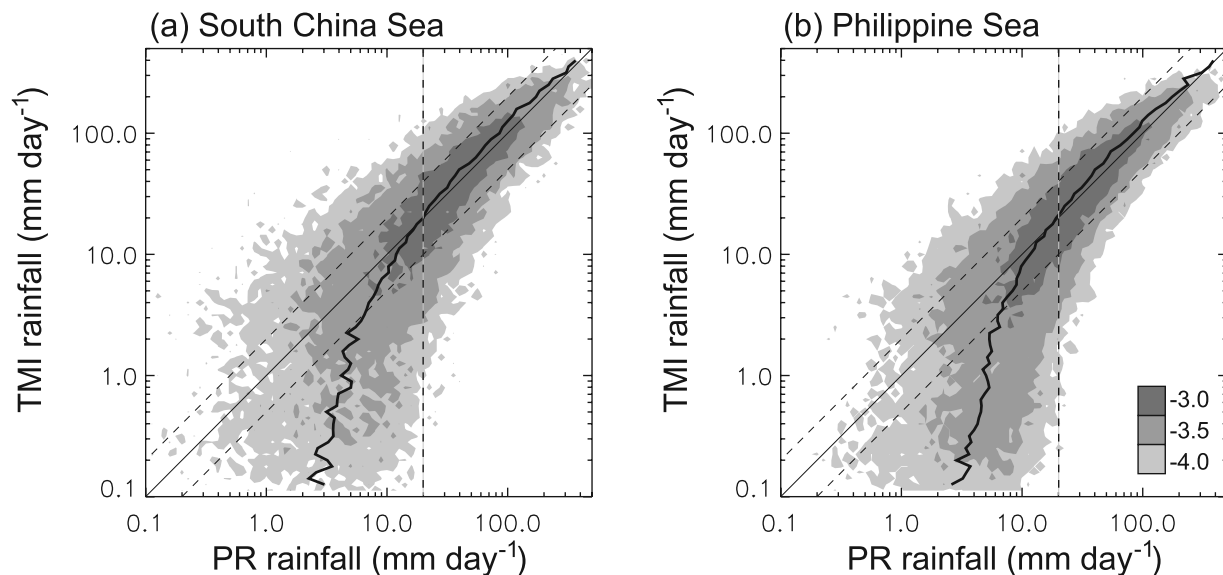


Figure 4. Contoured log frequency diagram of PR versus TMI rain rates (mm d⁻¹) for the JJA in 1998–2001: (a) the South China Sea and (b) the Philippine Sea. The median of the histogram is plotted (thick solid line); the solid and dashed thin lines are the 1:1 lines and 100% error lines, respectively. The vertical dashed lines indicate PR rain rate of 20 mm d⁻¹. The relative distribution is displayed as shaded contour; its color bar is in units of power of 10.

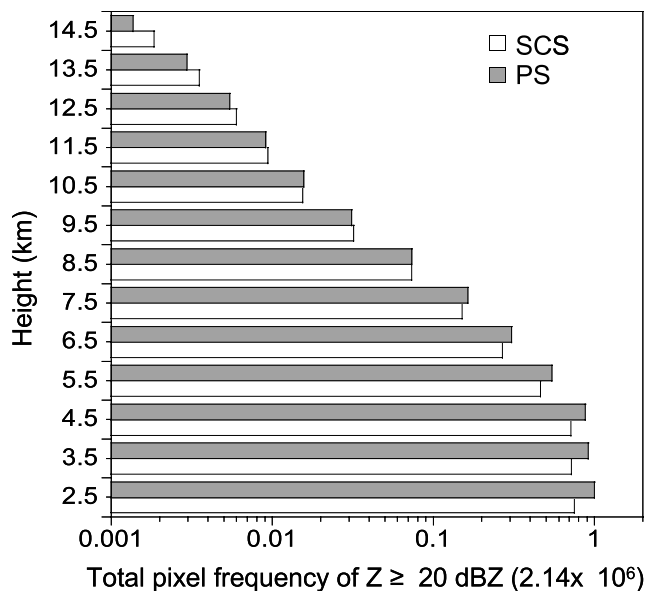


Figure 5. Total number of pixels with PR reflectivity greater than 20 dBZ with respect to height over the South China Sea and the Philippine Sea.

results evoke different cloud characteristics between the SCS and PS. We further explore PR reflectivity and TMI ice scattering signatures in the next two subsections.

4.2. PR Reflectivity

[27] PR reflectivity can be applied to examine the vertical structure of regional convection. As noted in section 2, radar reflectivity is a function of the sixth power of hydrometric diameter, the number of hydrometeors, and the dielectric factor related to the hydrometer phase; ice crystals have a lower dielectric factor than liquid water drops for the same diameter. Thus high PR reflectivity indicates the existence either of many particles or of large-sized particles. Further, PR is relatively insensitive to ice particles unless they are large enough to be detectable [Masunaga et al., 2002].

[28] Figure 5 shows the total number of pixels of PR reflectivity over 20 dBZ with respect to height over the SCS and PS. The counts of near-surface pixels are not the same, which is more frequent over the PS (2.14×10^6) than over the SCS (1.61×10^6). For a more quantitative comparison between the regions the histogram is normalized by dividing the count of near-surface pixels in the PS in Figure 5. The criterion of reflectivity, 20 dBZ, is selected because it is a sufficiently high value compared to PR detectability. The minimum detectable reflectivity is 17 dBZ from PR noise level (14 dBZ) from a general signal-to-noise ratio ($=1/3$, <http://trmm.gsfc.nasa.gov/>) and/or averaging of pulses from 120 to 250 m resolution [Iguchi et al., 2000]. The figure indicates that the total pixel number of reflectivity ≥ 20 dBZ is larger over the PS than over the SCS in the middle and lower troposphere, while the opposite is true in the upper troposphere. In comparison with the upper troposphere (5.88×10^{-4} at 14–15 km), the difference between the SCS and PS is 3 orders higher (2.46×10^{-1} at 2–3 km) in the lower troposphere because the total number itself is relatively large. However, this difference amounts to almost 25% of the total number for both altitudes 14–15 km and 2–3 km (i.e., 14.5 and 2.5 km in the y axis of Figure 5). Considering the tropical freezing level is about 5 km, rain is more frequent over the PS than over the SCS; rather, ice particles occur more frequently in the upper troposphere over the SCS than over the PS.

[29] Relative frequency distribution of the PR reflectivity (RFDR) is an indicator that represents the vertical structure of cloud in the given region [Petersen and Rutledge, 2001]. The relative frequency is calculated by dividing the total number of reflectivities ≥ 20 dBZ at each elevation. The RFDRs are displayed with respect to height in Figure 6. In the troposphere below the freezing level (<5 km), the RFDRs in the two regions have a similar character; RFDRs for ≥ 30 dBZ are relatively large compared to those in the upper layers. RFDRs ≥ 30 dBZ below the freezing level make up 61% and 73% of the total RFDRs for ≥ 30 dBZ in the whole troposphere for the SCS and PS, respectively. This indicates that precipitation mass dominates near the

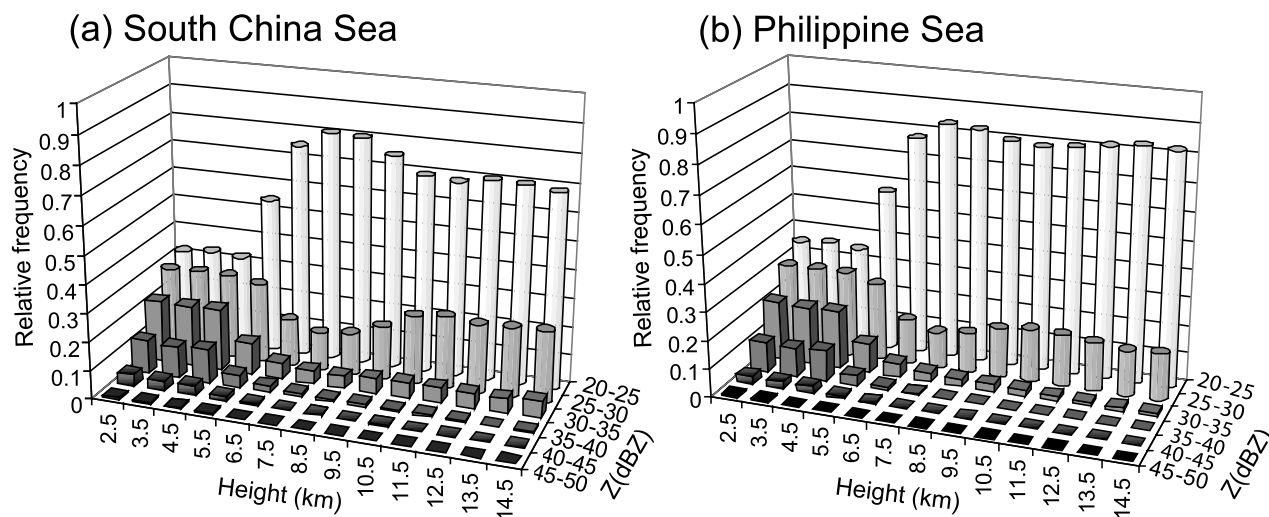


Figure 6. Relative frequency of PR reflectivity for (a) the South China Sea and (b) the Philippine Sea. The intensity of reflectivity (Z) is classified by every 5 dBZ and plotted on the y axis.

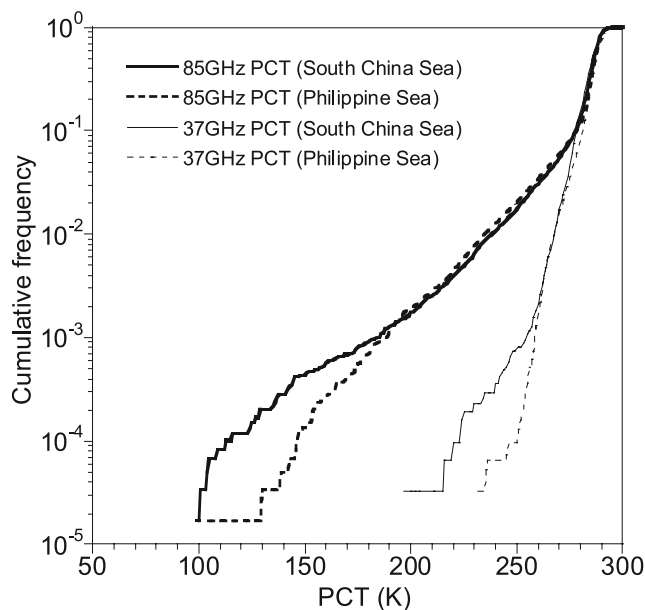


Figure 7. Cumulative frequency functions of TMI polarization corrected temperature (PCTs) at 37.0 GHz (thin line) and 85.5 GHz (thick line) for the South China Sea (solid line) and the Philippine Sea (dashed line).

surface over both the SCS and PS. With regard to heavy rainfall near surface (the lowest-level 2.5 km), the total of RFDRs ≥ 30 dBZ are 39% and 35% over the SCS and PS, respectively. Thus heavy rain is relatively frequent over the SCS compared to the PS, although overall rainfall is more frequent over the PS, as shown in Figure 5.

[30] Above a height of 6 km, however, the RFDR has a different pattern compared with the lower layers, so that the reflectivity of 20–25 dBZ takes a major portion. In detail, the RFDR 20–25 dBZ echoes over the SCS have a convex shape having a peak particularly at 7–8 km, while those over the PS are relatively flat. Moreover, the RFDR 25–30 dBZ echoes have a concave shape with a minimum at 7–8 km in the SCS and a flat distribution in the PS. These discrepancies of RFDRs (at both 20–25 and 25–30 dBZ) between the SCS and PS demonstrate that small raindrops and/or ice particles have vertically varied distribution over the SCS compared to those over the PS. On the other hand, Figure 6 shows that RFDRs of 30–35 dBZ over the SCS have similar quantities (~ 0.1) from the freezing level to the tropopause, while they are reduced gradually over the PS. Given the idea that the height of 30 dBZ echoes may be used as a measurement of convective intensity [Nesbitt *et al.*, 2000; Petersen and Rutledge, 2001], it is inferred from Figure 6 that convective intensity is relatively stronger in the SCS.

[31] Petersen and Rutledge [2001] classified cloud regime characteristics through analyzing various distributions of RFDRs over the globe: “continental” and “isolated oceanic” types. In the continental cloud regime, the convective region is more intense; and stratiform precipitation is more vertically developed, coupling with a frequent deep convective mode. As a result, the continental RFDRs generally represent a larger percentage of reflectivity ≥ 30 dBZ at levels above 5 km and a peak at 20–25 dBZ in the mid and upper troposphere (5–10 km altitude). By contrast, the

isolated oceanic RFDRs exhibit flat structure and weakened intensity with height. Therefore in summary, the cloud characteristic in the SCS is close to the continental type while in the PS it is close to the isolated oceanic type (see Figure 6). Accordingly, the role of ice in the precipitation process may be different between the SCS and PS; more ice particles with large diameter can develop over the SCS than over the PS.

4.3. Ice-Scattering Signature by TMI

[32] The TMI measured radiances are the integrated result of emission and scattering processes that act to modulate upwelling radiation along the optical path to the radiometer. At 85.5 and 37.0 GHz channels of the TMI, the scattering effect by ice particles is primary and the emission by liquid water is minor in determining the upwelling radiance [Spencer *et al.*, 1989]. The TMI microwave TB is converted to the polarization-corrected temperature (PCT) to minimize the effects of the underlying surface [Mohr and Zipser, 1996; Cecil *et al.*, 2002]. The PCTs at 85.5 and 37.0 GHz, respectively, are computed as follows [Spencer *et al.*, 1989]:

$$\text{PCT}_{85} = 1.82 \text{ TB}_{85V} - 0.82 \text{ TB}_{85H} \quad (1)$$

$$\text{PCT}_{37} = 2.20 \text{ TB}_{37V} - 1.20 \text{ TB}_{37H} \quad (2)$$

where V and H represent vertical and horizontal polarization, respectively. As ice scattering reduces the observed microwave TB, the PCTs have low values for optically dense ice particles (refer to equations (1) and (2)). Generally, $\text{PCT}_{85} \leq 250$ K and $\text{PCT}_{37} \leq 270$ K are regarded as significant ice scattering signatures at the corresponding frequencies (see Spencer *et al.* [1989] and Cecil *et al.* [2002] for more details). The magnitude of PCT depends on optical depth, which is a function of many factors including the wavelength, vertical distribution and concentration, phase, density, and size of hydrometeors [Cecil *et al.*, 2002]. It is noted that 85.5 GHz is more sensitive to smaller ice particles than 37.0 GHz.

[33] Figure 7 shows the cumulative frequency distributions of TMI PCT_{37} and PCT_{85} over the SCS and PS. Only common pixels of the TMI within the narrow PR swath are calculated because the TMI swath width includes that of the PR. The cumulative frequency is normalized by the total number of pixels passing over the domain. In Figure 7, the cumulative frequencies for $\text{PCT}_{85} \leq \sim 190$ K and $\text{PCT}_{37} \leq \sim 260$ K have large values in the SCS. Likewise, the difference is more obvious when the PCTs have very low values. The results suggest that strong ice scattering tends to occur more often over the SCS compared with the PS. Therefore the optical depth of ice particles over the SCS is thicker, which may be responsible for more active deep convection with a well-developed ice layer. The effect of beam filling on ice scattering possibly affects PCT, especially at 37.0 GHz where the footprint size is larger than the size of small convective clouds. Nevertheless, the consistent difference at 85.5 GHz, of having a smaller footprint size, suggests that the effect of beam filling would be secondary. In addition, for PCT_{85} between 190 K and 250 K, the cumulative frequencies over the PS are slightly more than over the SCS. However, this can be negligible because the emission

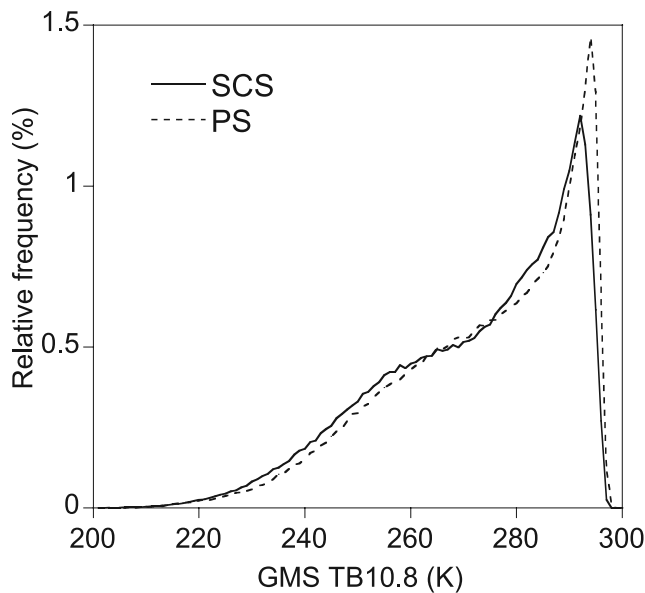


Figure 8. The relative frequencies (%) calculated by Geostationary Meteorological Satellite-5 (GMS-5) 10.8- μm brightness temperature (TBs) over the South China Sea (solid line) and the Philippine Sea (dashed line).

by cloud liquid water acts to increase TB, to some degree, at both 37.0 and 85.5 GHz by up to 10 K [Toracinta *et al.*, 2002].

5. Interpretation of Regional Dependence in TRMM Observations

[34] The excess of PR over TMI in conditional rainfall over the TNP is actually consistent with the version 5 results from Nesbitt *et al.* [2004] and Masunaga *et al.* [2002]; these earlier studies tried to link the bias to (1) the PR's attenuation correction causing low rain rates and (2) the TMI's overestimates over ocean in large rain volume features (systems with $>10^4 \text{ mm h}^{-1} \text{ km}^2$) with high stratiform rain fractions. With regard to the regional difference (i.e., PS > SCS in the PR–TMI bias), it can be explained by combining the above two reasons with the present results in sections 3 and 4. Firstly, the uncertainty in the PR's attenuation correction in heavy precipitation around tropical rainfall maxima may be larger over the SCS than over the PS. More frequent heavy rain events and higher rain rates were found over the SCS by the PR reflectivity and conditional rain rates (discussed in sections 4.1 and 4.2). In other words, the PR rain rate may be underestimated relative to the TMI. Secondly, a positive bias in TMI rain rate may become pronounced over the SCS by stronger emissions from the melting layer. Accordingly, the emissions, primarily by water-coated aggregates above the freezing level, can increase passive microwave rain rate retrievals especially in large features that have higher fractions of stratiform rain than in smaller ones [Nesbitt *et al.*, 2004]. This overestimation of rain rate by such emissions correlates positively with strong convective intensity and high cloud top height, which are dominant over the SCS, more than over the PS, in connection with mean vertical velocity, PR reflectivity, and TMI ice scattering (discussed in sections 3 and 4).

[35] Because the TRMM is a low-Earth orbiting satellite having a narrow swath of sensors, sampling frequencies may not be sufficient. In comparison to that, the GMS-5 distributes rather continuous observations with high time resolution on the spatially fixed region covering the TNP. TB at 10.8- μm band (hereafter TB_{10.8}) has long been considered a proxy of cloud top properties for optically thick clouds [Masunaga *et al.*, 2005]. For single-layer high clouds with an optical depth above about 2, their cloud top height, corresponding to TB_{10.8} < 245 K, is generally above 300 hPa [Choi *et al.*, 2005].

[36] Figure 8 shows the relative frequency distributions of GMS-5 TB_{10.8} over the two regions during the analysis period. Obviously, the frequency for low TB_{10.8} (<260 K) is higher for the SCS than for the PS. Therefore it is suggested that the SCS dominates the PS in the population of deep convection. This indicator of the dominance of deep convection over the SCS is consistent with stronger rain rates for heights >11 or 12 km over the SCS compared to the PS, as shown in Figure 5. In fact, the deep convective and stratiform events induced by deep convection are known to be primary contributors to rain probability or rainy area fraction over the west Pacific [Masunaga *et al.*, 2005, Figure 4]. However, it is less obvious to conclude that this result can directly explain smaller rainy area fraction over the SCS. In the calculation of rainy areas in the available data in this study, rainy areas are about 15% larger over the PS than over the SCS. This smaller fraction must be caused by topographic effects on westerlies passing over the Indochina peninsula [Xie *et al.*, 2003]. Heavy rainfall is observed in the peninsula and light rainfall around the east coast of the peninsula (Figures 1a and 3). In contrast, for cloud estimates from TB_{10.8} between 260 K and 280 K, the frequencies are comparable in the two regions. These clouds must contain both liquid and ice particles, because clouds typically do not glaciate until the temperature reaches around -15°C [Johnson *et al.*, 1999]. Note that the clouds can be regarded as cumulus congestus, which was defined as a cloud with a radar echo top height of 4–6 km and TB_{10.8} larger than 260 K [Masunaga *et al.*, 2005; Johnson *et al.*, 1999].

[37] In addition, videosonde measurements [Takahashi, 2006] showed more graupel at sites located in the SCS and fewer graupel over the broad region covering the PS. Accompanying lightning flashes also display regionally distinctive densities (Table 2). The averaged lightning densities of LIS are roughly 4 times higher over the SCS than over the PS in the JJA of 2000. The excess of graupel and lightning density over the SCS is certainly consistent with the deeper convection and heavier rainfall over the SCS found in this study. The analysis of PR RFDR and TMI PCT is a primary source of the evidence to support this feature. The stronger JJA-mean positive 500-hPa relative vorticity (or upward motion) over the SCS compared to the PS may also be explained in connection with the formation of deeper convection.

6. Summary and Discussion

[38] The present study explores regional cloud characteristics over the TNP. During summer, most parts of the TNP are covered by high SSTs (29–30°C), which provide

favorable conditions for an unstable atmosphere. In particular, common areas of positive vorticity and of strong upward motions appear separately over the SCS and the PS. CMAP rainfalls are concentrated in those two regions. Although similar potential temperature profiles are represented in the two regions, higher values of θ_e and θ_e^* are actually observed in the SCS. This may be mainly due to more moisture in the atmosphere overlying the SCS compared to the PS. Strong vertically integrated moisture flux convergence over China is observed near the SCS during summer [Simmonds et al., 1999].

[39] We first carried out the validation for the available TRMM data in this study: version 6 of TRMM products for JJA of the period 1998–2001. In regard to PR–TMI bias, conditional and unconditional rainfall averages show different features. The PR–TMI bias in the unconditional rainfall is very small ($<1 \text{ mm d}^{-1}$), while it is large ($>7 \text{ mm d}^{-1}$) in the conditional rainfall. The beam-filling effect and minimum rain rate sensitivity are much different between PR and TMI and thus affect the discrepancies. Although the overall rainfall bias in this study is somewhat reduced compared to version 5, the intensity of rainfall itself still indicates a large discrepancy between TMI and PR. This PR–TMI rainfall bias is smaller over the SCS compared to the PS, which is ultimately attributed to heavier rainfall, stronger convective intensity, and higher cloud top height over the SCS.

[40] On the basis of a higher frequency for PR reflectivity ($\geq 20 \text{ dBZ}$) by the tropopause and lower TMI PCT, it is concluded that the SCS dominates the PS in deeply developed cloud systems. More lighting density in LIS and more frequent low IR TB also supports this dominance of SCS over the PS. The rainfall area fraction is, however, about 15% smaller over the SCS compared to the PS.

[41] As more satellites will be launched in the future, targeting the distribution of precipitation, it will become more crucial to validate biases in satellite-based rainfall retrievals/climatologies due to regional differences in the precipitation process. The present study also attempts to link those rain biases with cloud activities in the TNP, and to make a comparison of regional cloud and rainfall characteristics. The imprecise simulations of convection over the areas under consideration in the various climate models have been pointed out in some previous studies [e.g., Kang et al., 2002]. Therefore the present study may be helpful in validating cumulus parameterization in climate modeling. However, this study is limited to climatology for the 4-year period of summers mentioned. So, more reliable studies, concerning annual variations related to El Niño/La Niña episodes or the Asian monsoon, should be further examined.

[42] **Acknowledgments.** This work was funded by the Korea Meteorological Administration Research and Development Program under grant CATER 2006-4204. The first and second authors were also supported by the BK21 project of the Korean government. The authors wish to thank H.-S. Lee, J.-J. Baik, and Y. Takayabu for giving valuable advice. The authors appreciate that NASA Goddard made the TRMM data sets freely available. The authors are grateful for the critical and valuable comments made by three anonymous reviewers.

References

- Berg, W., C. Kummerow, and C. A. Morales (2002), Differences between east and west Pacific rainfall systems, *J. Clim.*, *15*, 3659–3672.
- Berg, W., L. Ecuver, and C. Kummerow (2006), Rainfall climate regimes: The relationship of regional TRMM rainfall biases to the environment, *J. Appl. Meteorol.*, *45*, 434–454.
- Cecil, D. J., E. J. Zipser, and S. W. Nesbitt (2002), Reflectivity, ice scattering, and lightning characteristics of hurricane eyewalls and rainbands. Part I: Quantitative description, *Mon. Weather Rev.*, *130*, 769–784.
- Choi, Y.-S., C.-H. Ho, and C.-H. Sui (2005), Different optical properties of high cloud in GMS and MODIS observations, *Geophys. Res. Lett.*, *32*, L23823, doi:10.1029/2005GL024616.
- Christian, H. J., et al. (1999), The lightning imaging sensor, paper presented at the 11th International Conference on Atmospheric Electricity, NASA, Guntersville, Ala., 7–11 June.
- Iguchi, T., T. Kozu, R. Meneghini, J. Awaka, and K. Okamoto (2000), Rain-profiling algorithm for the TRMM Precipitation Radar, *J. Appl. Meteorol.*, *39*, 2038–2052.
- Johnson, R. H., T. M. Rickenbach, S. A. Rutledge, P. E. Ciesielski, and W. H. Schubert (1999), Trimodal characteristics of tropical convection, *J. Clim.*, *12*, 2397–2418.
- Kalnay, E., et al. (1996), The NCEP/NCAR 40-year reanalysis project, *Bull. Amer. Meteorol. Soc.*, *77*, 437–471.
- Kang, I.-S., et al. (2002), Intercomparison of the climatological variations of Asian summer monsoon precipitation simulated by 10 GCMs, *Clim. Dyn.*, *19*, 383–395.
- Kummerow, C., W. Barnes, T. Kozu, J. Shiue, and J. Simpson (1998), The Tropical Rainfall Measuring Mission (TRMM) sensor package, *J. Atmos. Oceanic Technol.*, *15*, 809–816.
- Kummerow, C., et al. (2000), The status of the Tropical Rainfall Measuring Mission (TRMM) after two years in orbit, *J. Appl. Meteorol.*, *39*, 1965–1982.
- Kummerow, C., et al. (2001), The evolution of the Goddard Profiling Algorithm (GPROF) for rainfall estimation from passive microwave sensors, *J. Appl. Meteorol.*, *40*, 1801–1820.
- Masunaga, H., T. Iguchi, R. Oki, and M. Kachi (2002), Comparison of rainfall products derived from TRMM Microwave Imager and Precipitation Radar, *J. Appl. Meteorol.*, *41*, 849–862.
- Masunaga, H., T. S. L'Ecuver, and C. D. Kummerow (2005), Variability in the characteristics of precipitation systems in the tropical Pacific. Part I: Spatial structure, *J. Clim.*, *18*, 823–838.
- Mohr, K. I., and E. J. Zipser (1996), Defining mesoscale convective systems by their 85 GHz ice-scattering signature, *Bull. Amer. Meteorol. Soc.*, *77*, 1179–1189.
- Nesbitt, S. W., E. J. Zipser, and D. J. Cecil (2000), A Census of precipitation features in the tropics using TRMM: Radar, ice scattering, and lightning observations, *J. Clim.*, *13*, 4087–4106.
- Nesbitt, S. W., E. J. Zipser, and C. Kummerow (2004), An examination of version-5 rainfall estimates from the TRMM Microwave Imager, Precipitation Radar, and rain gauges on global, regional, and storm scales, *J. Appl. Meteorol.*, *43*, 1016–1036.
- Petersen, W. A., and S. Rutledge (2001), Regional variability in tropical convection: Observations from TRMM, *J. Clim.*, *14*, 3566–3586.
- Reynolds, R. W., and T. M. Smith (1994), Improved global sea surface temperature analyses, *J. Clim.*, *7*, 929–948.
- Simmonds, I., D. Bi, and P. Hope (1999), Atmospheric water vapor flux and its association with rainfall over China in summer, *J. Clim.*, *12*, 1353–1367.
- Simpson, J., R. F. Adler, and G. R. North (1988), A proposed Tropical Rainfall Measuring Mission (TRMM) satellite, *Bull. Amer. Meteorol. Soc.*, *69*, 278–295.
- Simpson, J., C. Kummerow, W.-K. Tao, and R. Adler (1996), On the Tropical Rainfall Measuring Mission (TRMM), *Meteorol. Atmos. Phys.*, *60*, 19–36.
- Song, Y., E. A. Smith, K. S. Kuo, and W. S. Olson (2004), Standing discrepancies between TRMM version 6 rain rate retrieval algorithms, paper presented at the International Radiation Symposium, Seoul Natl. Univ., Busan, Korea, 23–28 Aug.
- Spencer, R. W., H. M. Goodman, and R. E. Hood (1989), Precipitation retrieval over land and ocean with the SSM/I: Identification and characteristics of the scattering signal, *J. Atmos. Oceanic Technol.*, *6*, 254–273.
- Takahashi, T. (2006), Precipitation mechanisms in east Asian monsoon: Videosonde study, *J. Geophys. Res.*, *111*, D09202, doi:10.1029/2005JD006268.
- Toracinta, E. R., D. J. Cecil, E. J. Zipser, and S. W. Nesbitt (2002), Radar, passive microwave, and lightning characteristics of precipitation systems in the Tropics, *Mon. Weather Rev.*, *130*, 802–824.
- TRMM PR Team (2005), Tropical Rainfall Measuring Mission (TRMM) Precipitation Radar Algorithm Instruction Manual for version 6, 180 pp., Jpn. Aerosp. Explor. Agency (JAXA), Tokyo–NASA, Washington, D. C.

- (Available at http://www.eorc.jaxa.jp/TRMM/document/pr_manual/pr_manual_v6.pdf)
- Wilheit, T. T. (1986), Some comments on passive microwave measurement of rain, *Bull. Amer. Meteorol. Soc.*, *67*, 1226–1232.
- Wu, R., and J. A. Weinman (1984), Microwave radiances from precipitating clouds containing aspherical ice, combined phase, and liquid hydrometeors, *J. Geophys. Res.*, *89*, 7170–7178.
- Xie, P., and P. A. Arkin (1997), Global precipitation: A 17-year monthly analysis based on gauge observations, satellite estimates and numerical model outputs, *Bull. Amer. Meteorol. Soc.*, *78*, 2539–2558.
- Xie, S., Q. Xie, D. Wang, and W. T. Liu (2003), Summer upwelling in the South China Sea and its role in regional climate variations, *J. Geophys. Res.*, *108*(C8), 3261, doi:10.1029/2003JC001867.
-
- M.-H. Ahn, Meteorological Research Institute, Korea Meteorological Administration, Seoul 156-720, Korea.
- Y.-S. Choi, C.-H. Ho, and M.-S. Park, School of Earth and Environmental Sciences, Seoul National University, Seoul 151-742, Korea. (hoch@cpl.snu.ac.kr)
- S. K. Park, Department of Environmental Science and Engineering, Ewha Womans University, Seoul 120-750, Korea.
- C.-H. Sui, Institute of Hydrological Sciences, National Central University, Jhongli City, Taoyuan, Taiwan 320.